2019

Crystal plasticity modelling of microbands in a rolled aluminium single crystal

Hui Wang
University of Wollongong, University of Tokyo, huiw@uow.edu.au

Cheng Lu
University of Wollongong, chenglu@uow.edu.au

Anh Kiet Tieu
University of Wollongong, ktieu@uow.edu.au

Crystal plasticity modelling of microbands in a rolled aluminium single crystal

Abstract

In this study, an aluminium single crystal was deformed by roll-bonding, and the through-thickness texture and microstructure were characterized by electron backscattered diffraction (EBSD). Matrix bands and transition bands developed at the macro-scale, and microbands formed at the lower scale. Moreover, the crystal plasticity finite element method (CPFEM) was used to model the experimentally observed macro- and micro-subdivision. Matrix bands were captured in the Globalmodel that had a coarse mesh, and Submodel was adopted to predict microbands by refining the mesh. Two smaller regions of interest were selected from the Globalmodel and they were reconstructed in the Submodel. The Submodel was finely meshed, and it was deformed by the displacement-solution saved in the Globalmodel. One primary set of microbands in matrix bands and two sets of microbands in transition bands were successfully predicted. The deformation history at two points were traced to investigate the formation of microbands. The dominance of microbands in the Submodel was found to be associated with slip activity in the Globalmodel, and the formation and crystallographic nature of microbands were studied.

Disciplines

Engineering | Science and Technology Studies

Publication Details

Wang, H., Lu, C. & Tieu, K. (2019). Crystal plasticity modelling of microbands in a rolled aluminium single crystal. Materialia, 8 100488-1-100488-7.

Crystal plasticity modelling of microbands in a rolled aluminium single crystal

Hui Wang[1,2,*], Cheng Lu[1], Kiet Tieu[1]

1. School of Mechanical, Materials, Mechatronic, and Biomedical Engineering, University of Wollongong, New South Wales 2522, Australia

2. Research Center for Advanced Science and Technology, The University of Tokyo, Japan

*Corresponding author. hw737@uowmail.edu.au (H.Wang)

Abstract: In this study, an aluminium single crystal was deformed by roll-bonding, and the through-thickness texture and microstructure were characterized by electron backscattered diffraction (EBSD). Matrix bands and transition bands developed at the macro-scale, and microbands formed at the lower scale. Moreover, the crystal plasticity finite element method (CPFEM) was used to model the observed macro- and micro-subdivision in the corresponding experiment. Matrix bands were captured in the Globalmodel that had a coarse mesh, and after this a modelling skill, Submodel, was adopted to better balance the computation time and prediction. Two smaller regions of interest were selected from the Globalmodel and they were reconstructed in the Submodel. The Submodel was finely meshed, and it was deformed by the displacement-solution saved in the Globalmodel. One primary set of microbands in matrix bands and two sets of microbands in transition bands were successfully predicted. The deformation history at two points were traced to investigate the formation of microbands. The dominance of microbands in the Submodel was found to be associated with slip activity in the Globalmodel, and the favour and crystallographic nature of microbands were studied.

Keywords: Crystal plasticity FEM; Microbands; Submodel; Mesh resolution; Subdivision

1. Introduction

During plastic deformation, the crystal orientations in single crystals or grains of polycrystals rotate in different directions or in the same direction but with different rotation magnitudes. These differences in crystal rotation result in subdivision [1]. The subdivision is manifested by different deformation features at various length-scales [2]. For instance, matrix bands are one of the most prevail features at the macro-scale [3], and microbands at a lower scale [4]. An

extensive collection of experimental studies have been conducted to study matrix bands and microbands in rolled single crystals [3, 5]. The direction of crystal rotation and slip activities in a matrix band remain constant [3, 5], but change between adjacent matrix bands. In rolling, the boundaries between matrix bands are along the rolling direction (RD) [3, 5], which have continuously varying crystal orientations and thus are called transition bands. As for microbands, they usually form in two sets due to the activation of two sets of slip systems and incline at $\pm 30^{\circ} \pm 5^{\circ}$ to the RD [4]. The formation of microbands is due to the cyclic fluctuation of slip activities along the RD. Matrix bands and microbands have been well experimentally characterized, but the formation history of them has not been explicitly revealed and spatially resolved.

As an alternative of experimental characterization techniques, crystal plasticity (CP) modelling provides access to the whole deformation history. The CP modelling has become a well-established method to study material subdivision, local heterogeneities, slip activities, and texture evolution. Various CP models have been proposed, and they can be roughly categorized into three groups, uniform-filed theory (e.g., Taylor model), mean-field theory (e.g., self-consistent model), and full-field theory. Compared to the first two groups, no homogenization is assumed in the crystal plasticity finite element method (CPFEM), a full-field theory. In CPFEM, the CP constitutive law is incorporated into the finite element method (FEM), and in each FEM increment the strain compatibility and stress equilibrium are reached at the same time for all elements. This is why the computation time of CPFEM simulations is usually large. Because of no homogenization, one advantage of the CPFEM model over those in the other two groups is that it can accurately access to grain interaction, intra-grain subdivision, and heterogeneous deformation, etc. Matrix bands were successfully captured by the CPFEM model in rolled single crystals, e.g., {0 0 1}<1 0 0> [6] and {1 1 2}<1 1 1> [7]. In contrast, the formation of microbands has not been extensively investigated by the CP models. Using CPFEM model, Dmitrieva *et al* [8] modelled the lamination microstructure in a shear deformed copper single crystal, but the lamination microstructure was not well spatially resolved due to the low mesh resolution. Wang *et al* [9] predicted the lamination formation by the crystal plasticity fast Fourier transformation (CPFFT) with a sufficient resolution, but the CPFFT model, a full-field theory, is only applicable to periodic boundary conditions. One reason that microbands have not been explicitly revealed by the CPFEM model is that the

element size is usually much larger than the dimension of microbands, since subdivision within elements is not accessible. However, reducing element size in CPFEM simulations is tightly restricted by the fast increasing computation time.

In this report, the CPFEM model was used to study the formation of matrix bands and microbands in a rolled aluminium single crystal. The through-thickness matrix bands were successfully predicted in the Globalmodel. Submodel was used to improve the mesh resolution in smaller regions of interest, by which microbands were successfully captured. To validate the predictions, a corresponding experiment of rolled aluminium single crystals was performed, and the through-thickness texture and microstructure were characterized by electron backscattered diffraction (EBSD). After the validation, the history of microband formation and crystallographic nature of microbands were studied.

2. Experiment procedure

The starting material used in this work was (0 0 1)[1 0 0] Cube oriented aluminium single crystals of high purity (99.99%), and they were deformed by roll-bonding at 50% reduction. The initial dimensions of the sheets were 50 mm×10 mm×1 mm (length×width×thickness). Two sheets were stacked after the contacting surfaces being degreased and wire-brushed, and then they were joined by metal wires at the four corners. The stacked sheets were roll-bonded under dry conditions on a laboratory rolling mill consisting of 125 mm diameter rolls. The sheets were cooled in icy water immediately after roll-bonding. EBSD was performed on a JEOL-JSM7001F to characterize the through-thickness texture and microstructure. The EBSD observations were conducted at accelerating voltage of 15 kV, and a working distance of 15 mm. The EBSD samples were cut from the centre of the deformed sheets and the EBSD scans were performed on the RD-normal direction (ND) plane. The observed surface was mechanically ground and electropolished (16℃, 25V, and A3 Struers electrolyte). The EBSD scanned region covered 200 μm along the RD and the whole thickness along the ND, and the step size was 2 μm. To better characterize microbands, a smaller step size of 0.2 μm was applied to a reduced region.

3. Modelling method

The simulation was designed to match the experiment. A commercial FEM code, ABAQUS/Standard ver.6.9, was used to perform the simulation. A two-dimensional model under the assumption of plane strain deformation was developed, as shown in Fig.1a. The rolls were considered as analytical rigid bodies with a diameter of 125mm. After testing various coefficients, 0.25 was used to describe the friction between rolls and sheets because it provided the best match of textures. The roll-bonding was approximated by conventional rolling in the simulation, since the two stacked sheets in the experiment were joined by metal wires at the four corners and thus the relative displacement between them was negligible. The starting sheet (2 mm in thickness) was rolled to 1mm by 50% reduction. The initial orientation (0 0 1)[1 0 0] was assigned to all elements at the very beginning of the simulation. The element ID was CPE4R, which provides efficient and fast numerical formulation. The shape of elements was square, and the element size was 62.5 μm×62.5 μm after mesh calibration. This element size was much larger than the step size of EBSD scans used in the corresponding experiment, but further reducing element size was constrained by the computation capability. The simulation was applied to the whole sheet, and thus this simulation model is called Globalmodel in the following. After the simulation with the Globalmodel, two smaller regions marked with red edges in Fig.1a were selected from the Globalmodel, to which Submodel was applied to better balance the mesh resolution and computation time. Only the selected regions, not the whole sheet, in their initial configurations (i.e., undeformed state) were reconstructed in the Submodel. Two mesh refinement ratios, 1:400 and 1:1600, were used in the Submodel, where one element in the Globalmodel was respectively remeshed into 400 and 1600 elements in the Submodel, and thus the element sizes were 3.1 μm×3.1 μm and 1.6 μm×1.6 μm, comparable to the EBSD step size. The time-dependent solution saved in the Globalmodel was applied to the boundaries of the Submodel to deform the material in the Submodel. The degrees of freedom and initial orientation of the Submodel were the same as those in the Globalmodel.

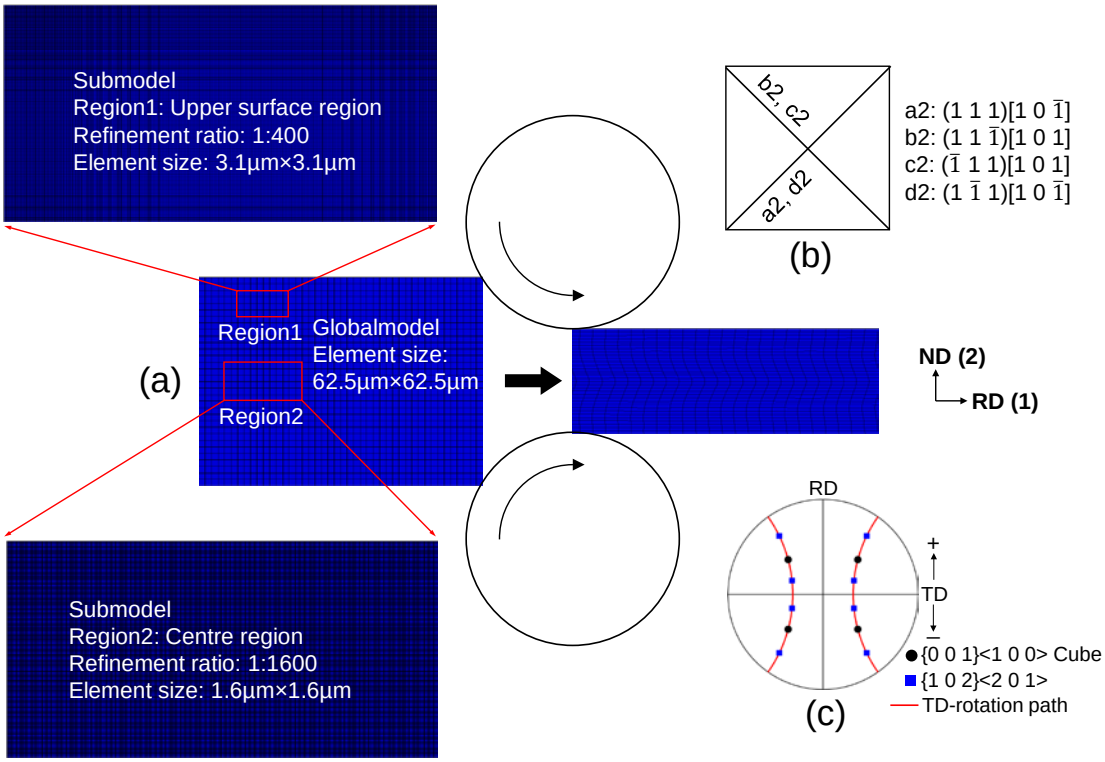

Fig.1. (a) Relation between Globalmodel and Submodel, (b) distribution of four primarily activated slip systems in (0 0 1)[1 0 0] Cube, and (c) a {1 1 1} pole figure shows the positions of the starting orientation (Cube) and {1 0 2}<2 0 1>, and TD-rotation path.

A well-recognized kinematic scheme [10] was adopted in this CPFEM model. In this scheme, crystallographic slip and lattice rotation are the two mechanisms for deformation, and the lattice rotation is the reason for texture evolution. The material spin $\mathbf{\Omega}$ is composed of two parts, $\mathbf{\Omega}^{\mathrm{p}}$ and $\mathbf{\Omega}^{\mathrm{e}}$, i.e.,

$$\mathbf{\Omega} = \mathbf{\Omega}^{\mathrm{P}} + \mathbf{\Omega}^{\mathrm{e}} \tag{1}$$

where $\mathbf{\Omega}^{\mathrm{p}}$ and $\mathbf{\Omega}^{\mathrm{e}}$ are plastic spin and lattice spin, respectively. The plastic spin $\mathbf{\Omega}^{\mathrm{P}}$ results from crystallographic slip, during which the crystal orientation keeps unchanged. The plastic spin can be calculated by

$$\mathbf{\Omega}^{\mathrm{p}} = \sum_{\alpha=1}^{12} \frac{1}{2}\left(\mathbf{s}^{(\alpha)} \cdot \mathbf{m}^{(\alpha)} - \mathbf{m}^{(\alpha)} \cdot \mathbf{s}^{(\alpha)}\right)\dot{\gamma}^{(\alpha)} \tag{2}$$

where $\mathbf{s}^{(\alpha)}$ is the slip direction of slip system α and $\mathbf{m}^{(\alpha)}$ is the slip plane normal to α.

This kinematic scheme was implemented into ABAQUS/Standard by the user-defined material (UMAT) subroutine. The Bassani-Wu hardening model [11], a rate-dependent hardening

model, was employed. The material parameters in the hardening model were evaluated by fitting the simulated stress-strain curve with the experimental measurement of aluminium single crystals under plane strain compression. The details of CP theory, CPFEM implementation, hardening model, and material parameters have been given in Ref. [12]. This CPFEM model and the set of material parameters have been used to study texture evolution under different rolling techniques [12, 13] and accurate predictions have been obtained. 12 {1 1 1}<1 1 0> slip systems were assumed for aluminium. The primarily activated slip systems in Cube are a2, b2, c2, d2, and the distribution of them is shown in Fig.1b. The activation of these four slip systems would result in crystal rotation about the transverse direction (TD), and the TD-rotation path is expressed by a {1 1 1} pole figure in Fig.1c. Crystal rotation in the clockwise direction about the TD is termed as positive and marked as '+', while it is negative ('-') for anticlockwise rotation.

4. Results

Fig.2a shows the EBSD map of inverse pole figure (IPF) through the whole thickness after roll-bonding, and its corresponding {1 1 1} pole figure is shown in Fig.2e. It can be seen from Fig.2e that the main crystal rotation is about the TD-axis, while RD- and ND-rotation are very low. The deformation texture is mainly concentrated at {1 0 2}<2 0 1> expressed in Fig.1c. The TD-rotation in the clockwise and anti-clockwise directions resulted in the formation of two matrix bands ('M'), M1 and M2 in Fig.2a. The matrix bands and slip trace are nearly symmetrical about the bonded interface. The distribution of matrix bands (M1-M2) in this study is quite different from that (M1-M2-M1-M2) in another experimental study of rolled Cube single crystals [3]. This difference is believed to be caused by the difference in rolling bite geometry and friction conditions.

The slip traces within matrix bands are associated with the formation of microbands. One set of microbands is dominant in each matrix band (Fig.2a), which is called primary microbands. The primary microbands (or primary slip trace) in M1 are almost along the slip system set of b2-c2, while they are along a2-d2 in M2, as schematically shown in Fig.2b. The two sets of slip trace are almost equivalent at the surfaces in Fig.2b. Fig.2f shows the variation of misorientation angles along the Line1 marked in Fig.2a, where the angle is the value relative to the first point. The misorientation varies greatly along the line, i.e., crossing primary

microbands, and this led to the formation of a block structure, as schematically shown in Fig.2b. A step size of 0.2 μm was applied to a smaller region marked in Fig.2a, and the EBSD map of IPF is shown in Fig.2c. It can be seen that secondary microbands developed within primary ones, which are schematically represented by thin lines in Fig.2d. The secondary microbands are along the a2-d2, while the primary ones are along the b2-c2. Compared to the primary microbands, the secondary ones are more regular. Fig.2g shows the variation of misorientation angles (relative to the first point) along the Line2 marked in Fig.2c, i.e., crossing secondary microbands. The variation of misorientaiton angles along the Line2 is relatively lower than that along the Line1. The formation of secondary microbands resulted in a block-cell structure (Fig.2c, d).

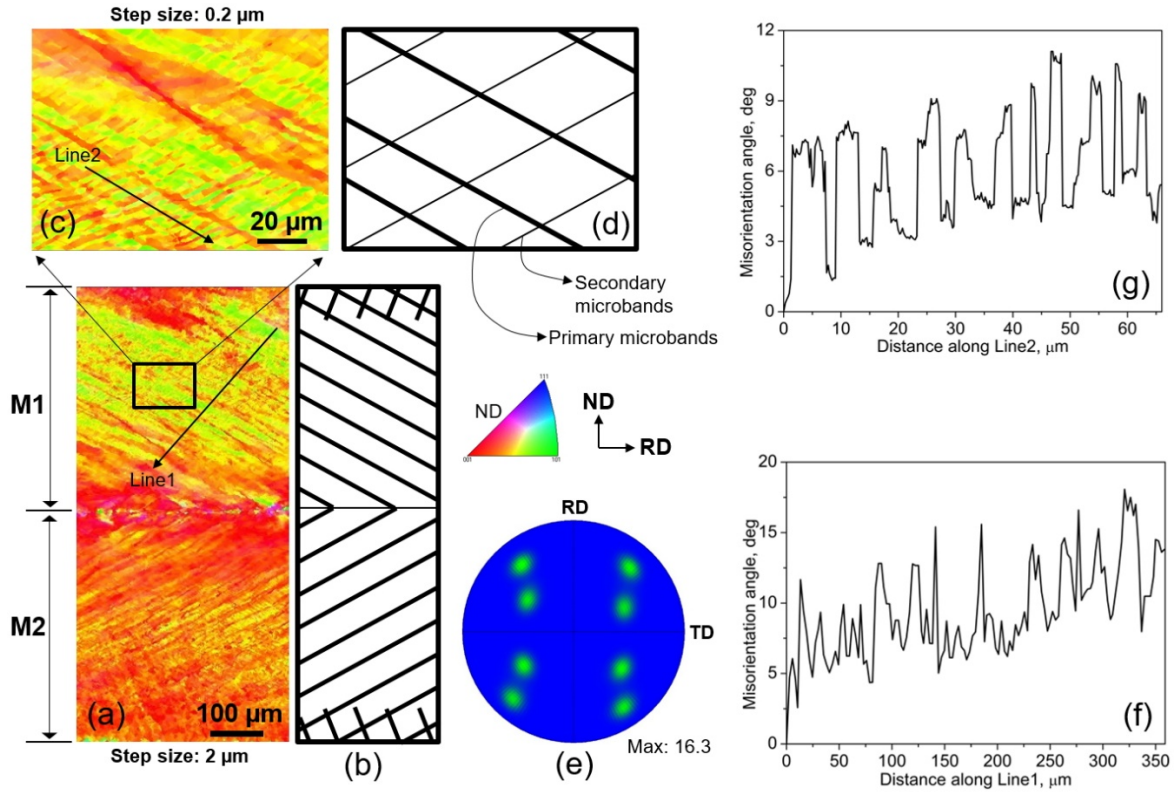

Fig.2. (a, b) EBSD maps of IPF and schematic drawings of slip trace through the whole thickness, and (c, d) in a smaller region. (e) A {1 1 1} pole figure constructed from the EBSD map in (a). (f, g) Misorientation (relative to the first point) along the Line1 marked in (a) and Line2 marked in (c).

As for CPFEM predictions, Fig.3a shows the distribution of predicted crystal rotation (or misorientation relative the starting orientation) in the Globalmodel. The crystal rotation is almost uniform along the RD, but it varies greatly through the thickness, and it is very low at

the centre and surfaces. Fig.3c shows the corresponding {1 1 1} pole figure, which was constructed by Matlab toolbox MTEX [14]. Similar to the experimental observation (Fig.2e), TD-rotation is also dominant in Fig.3c and the texture is concentrated at {1 0 2}<2 0 1>, while non-TD-rotation is very low. The simulated slip trace of the most highly activated slip system is expressed by a segment of straight lines on the RD-ND plane (Fig.3b), and the slip trace is centred at the centres of elements and the relative magnitude of cumulative shear strain on the slip systems is presented by the length of the segments. The simulated slip trace has been widely used to express the slip activities and represent microstructural features (e.g., Ref. [15]). Slip systems b2-c2 were primarily activated in M1 (Fig.3b), and a2-d2 in M2. The primary slip system set changes at the centre and surfaces, and the positions where this change occurred have relatively lower crystal rotation (Fig.3a). The predicted crystal rotation and simulated slip trace by the Globalmodel agree well with the experimental observations Fig.2a and e.

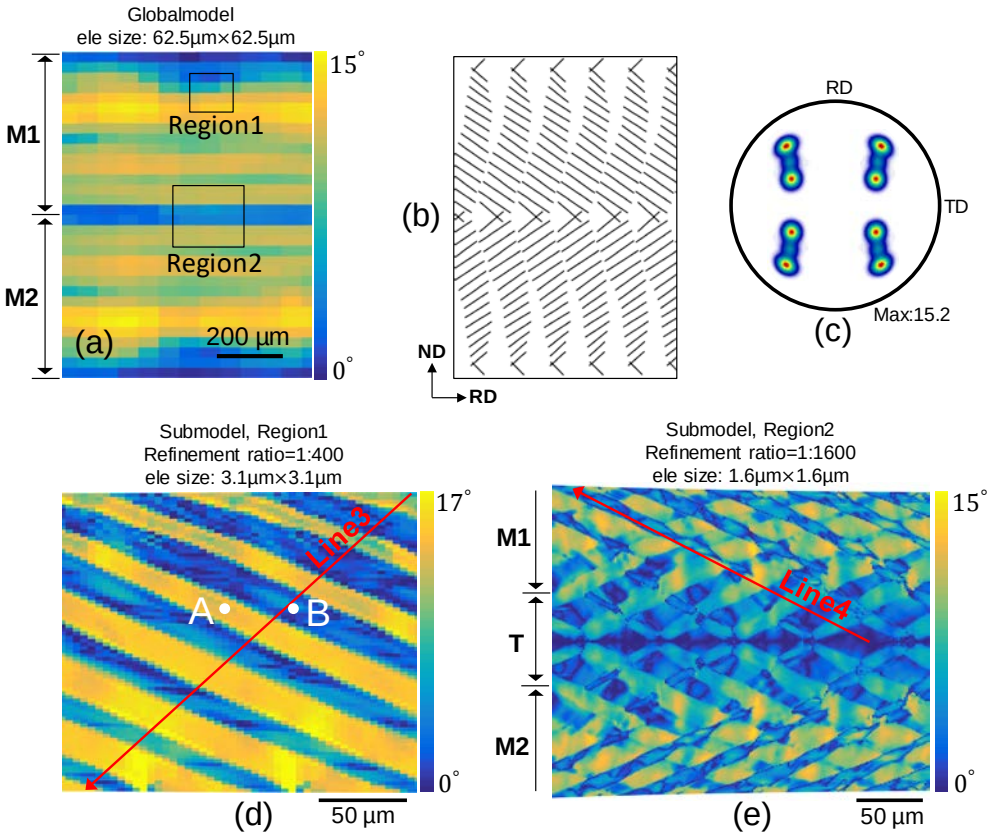

Fig.3. (a) Distribution of crystal rotation, (b) simulated slip trace, and (c) a {1 1 1} pole figure in the Globalmodel with an element size of 62.5 μm×62.5 μm. Distribution of crystal rotation

in the Submodel with refinement ratios of (d) 1:400 in the Region1, and (e) 1:1600 in the Region2.

Microbands were successfully predicted in the Submodel when the element size was reduced to 3.1 μm×3.1 μm (Fig.3d). The primary microbands are along the b2-c2 direction, similar to those in the experiment (Fig.2a and c) and slip trace in the Globalmodel (Fig.3b). Secondary microbands were not captured in Fig.3d, and also not in the Submodel with the mesh refinement of 1:1600 (not shown here). The formation of primary microbands resulted from the variation of crystal rotation along the RD, and the change of crystal rotation at microband boundaries is very sharp, similar to the experimental observations. When the element size was reduced to 1.6 μm×1.6 μm, the prediction of microbands was improved in the Submodel of Region2 (Fig.3e). The microband boundaries become smoother than those in Submodel of Region1. In Fig.3e, the microbands in M1 are along b2-c2, and a2-d2 in M2. Both primary and secondary microbands were successfully revealed in the transition band ('T'), where the primary and secondary microbands were alternated in the experiment (Fig.2a) and Globalmodel (Fig.3c). The previously developed microbands were slightly destroyed by the new developed ones, which resulted in the mutual offset between them.

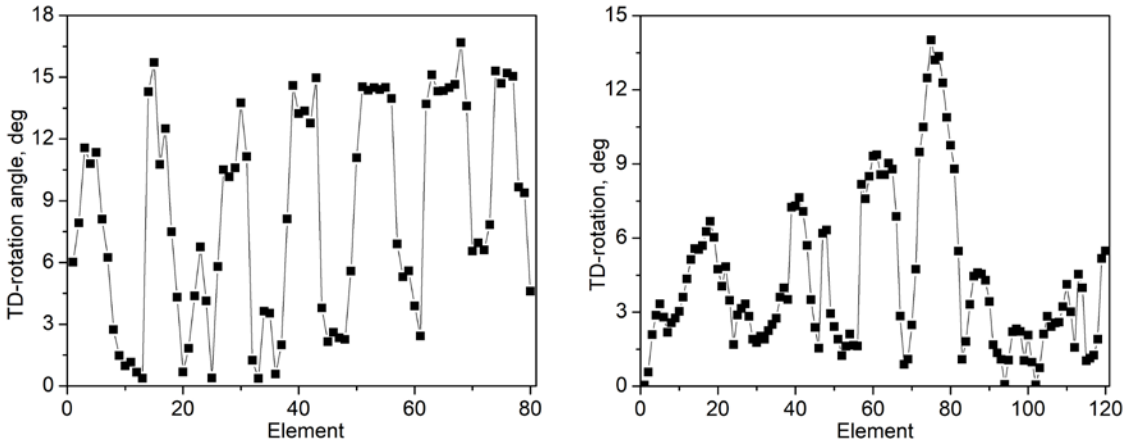

Fig.4. Distribution of TD-rotation angles along (a) Line3 and (b) Line4 marked in Fig.3.

Fig.4a shows the distribution of TD-rotation along Line3 marked in Fig.3d. This line runs cross the primary microbands, similar to Line1 (Fig.2a, g) in the experiment. Fig.4b shows the variation of TD-rotation along Line4 marked in Fig.3e, and this line crosses secondary microbands, comparatively to Line2 in Fig.2c, f. TD-rotation varies greatly along Line3, while

it is obviously lower along Line4. Compared to Fig.4b, the distribution of TD-rotation is relatively regular in Fig.4a. These predictions in Fig.4 are consistent with the experimental observations in Fig.2f, g. It needs to be noted that the TD-rotation in Fig.4 is the rotation relative to the starting orientation (Cube), while in the experiment it is the misorientation relative to the starting point (not starting orientation). This is why the TD-rotation angles in Fig.4 are slightly higher than those in Fig.2f, g. The TD-rotation is very high at ~Element 80 in Fig.4b, probably this position is located at a primary microband. These comparisons show that the predicted micro-subdivision in Fig.4 quantitatively match the experimental observations.

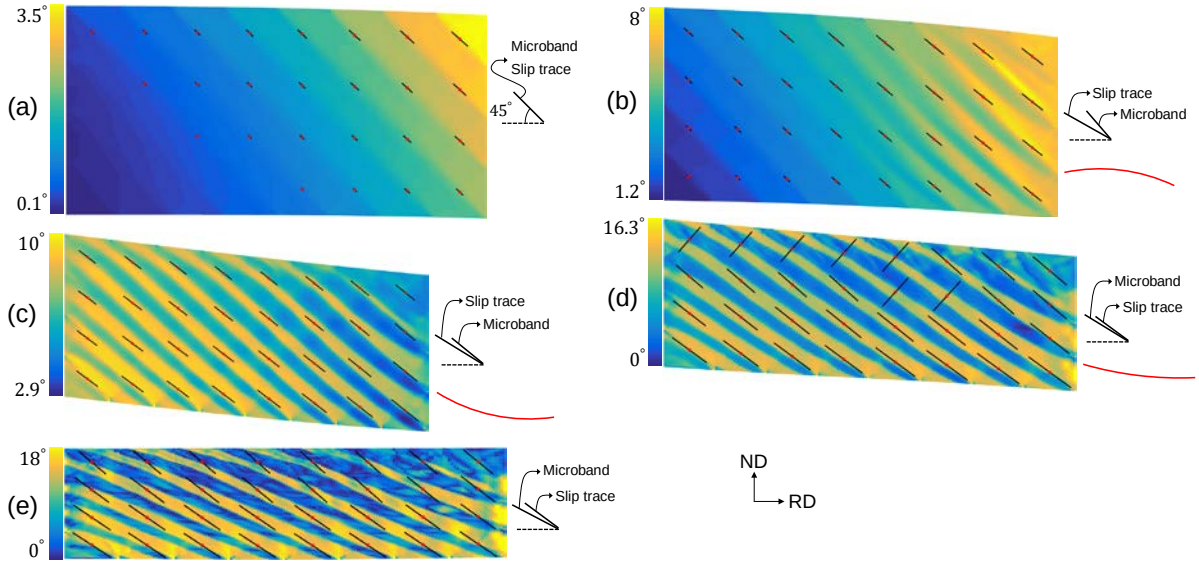

Fig.5. Evolution of crystal rotation in the Submodel of Region1 as a function of rolling time, (a) 2.12s, (b) 2.13s, (c) 2.15s, (d) 2.2s, and (e) 2.35s, where the simulated slip trace is from the corresponding region in the Wholemodel. The relative inclination of microbands and slip traces are schematically shown by black lines on the right hand, and the curved red lines indicate the bend of the Submodel.

Fig.5a-e shows the formation history of microbands in Region1 as a function of rolling time, which are characterized by crystal rotation in the Submodel and simulated slip traces of the corresponding region in the Globalmodel. The centres of simulated slip traces are marked by red points. Only the slip traces that have a cumulative shear strain on the most highly activated slip system over 0.005 is shown in Fig.5a-e. At 2.12s (Fig.5a), slip systems at the lower left corner were not activated in the Globalmodel, and microbands in the Submodel did not develop there too. The evolved slip traces are due to the activation of b2-c2, and they are

parallel with the developed microbands. At 2.13s (Fig.5b), slip traces developed in all elements in the Globalmodel. An angle developed between the microbands and slip traces, as schematically shown on the right hand. This angle is relatively obvious at the upper right corner, where the deformation is relatively larger. This angle is due to the bend of the Submodel, which is schematically represented by a curved red line. This angle became smaller at 2.15s (Fig.5c) due to the opposite bend of the Submodel. Because of the continuous bending, the inclination of microbands became smaller than that of slip trace at 2.2s (Fig.5d). This angle is slightly larger at 2.35s (Fig.5e), and the microbands and slip traces are not parallel after rolling. A small angle between microbands and plane has been observed in a large number of metals [16, 17]. However, in other researches [18, 19] microbands are found to be aligned with the highly stressed slip systems.

5. Discussion

The deformation in this experiment is featured by formation of matrix bands at the macro-scale, and microbands at the micro-scale. The development of matrix bands was predicted in the Globalmodel, and microbands were captured in the Submodel with greatly increased mesh resolution. To investigate the microband formation, the deformation history of two points, A and B marked in Fig.3d, was traced and is shown in Fig.6. The texture evolution at these two points will be briefly explained based on the CPFEM theory. The slip system activation results in plastic spin ($\mathbf{\Omega}^{\mathrm{P}}$) according to Eq. (2), while the shear strain represents the material spin ($\mathbf{\Omega}$), and the TD-rotation is lattice spin ($\mathbf{\Omega}^{\mathrm{e}}$). The relation between $\mathbf{\Omega}^{\mathrm{P}}$, $\mathbf{\Omega}^{\mathrm{e}}$, and $\mathbf{\Omega}$ is $\mathbf{\Omega} = \mathbf{\Omega}^{\mathrm{P}} + \mathbf{\Omega}^{\mathrm{e}}$, as expressed by Eq. (1). When the $\mathbf{\Omega}^{\mathrm{P}}$ is enough to meet the imposed $\mathbf{\Omega}$, $\mathbf{\Omega}^{\mathrm{e}}$ is not required. This kind of deformation, simultaneous change of $\mathbf{\Omega}^{\mathrm{P}}$ and $\mathbf{\Omega}$, is marked by red dashed lines in Fig.6. $\mathbf{\Omega}^{\mathrm{e}}$ evolves if $\mathbf{\Omega}^{\mathrm{P}}$ cannot meet $\mathbf{\Omega}$, which means all three variables change, as marked by green dashed lines. The blue dashed lines indicate the rolling time when $\mathbf{\Omega}^{\mathrm{P}}$ and $\mathbf{\Omega}^{\mathrm{e}}$ equally contribute to $\mathbf{\Omega}$, but in the opposite direction, and thus $\mathbf{\Omega}$ remains almost unchanged. For most cases marked by black dashed lines, only $\mathbf{\Omega}^{\mathrm{e}}$ contributes to $\mathbf{\Omega}$. At point A, the slip system set a2-d2 is highly activated over b2-c2 set almost during the whole rolling period, while the shear strain on a2-d2 set at point B is slightly higher than that on b2-c2 set. Therefore, $\mathbf{\Omega}^{\mathrm{P}}$ at point A and B is in the opposite direction. The $\mathbf{\Omega}$ is also opposite at point A and B, so the crystal rotation at both A and B is in the same direction (positive). However, the

magnitude of crystal rotation at A and B is different, and this leads to the formation of microbands, i.e., subdivision.

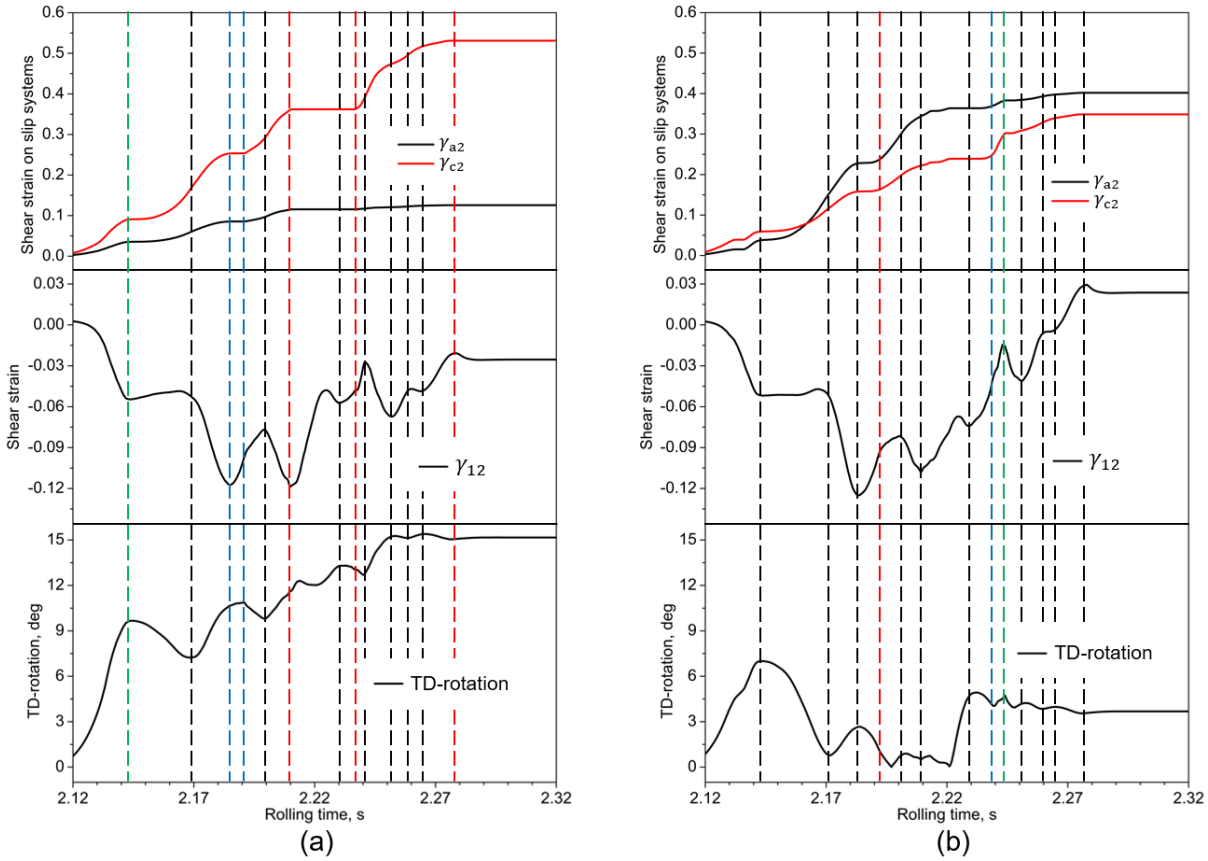

Fig.6. Deformation history of shear strain on slip systems, shear strain, and TD-rotation at point (a) A, and (b) B. The black dashed lines indicate the simultaneous change of shear strain and TD-rotation, red dashed lines for simultaneous change of shear strain and slip system activation, blue dashed lines for simultaneous change TD-rotation and slip system activation, and green dashed lines for simultaneous change of all three components (slip system activation, shear strain, and TD-rotation).

In rolling, the imposed deformation is not gradient-free, as demonstrated by the change of shear strain γ_{12} with rolling time (Fig.6). This change is due to the combined effect of rolling bite geometry and surface friction. Meanwhile, the stress also fluctuates during rolling, as can be seen from the change of slip activities (Fig.6), since according to the adopted rate-dependent hardening model [12] the slip system activation is solely determined by the resolved shear stress relative to the strength of slip systems (i.e., critical resolved shear stress, CRSS). The stress and strain fluctuation during rolling would respectively result in different

slip system activation ($\boldsymbol{\Omega}^{\mathrm{P}}$) and martial spin ($\boldsymbol{\Omega}$), and thus variation of crystal rotation ($\boldsymbol{\Omega}^{\mathrm{e}}$) according to Eq. (1). Subdivision is not predicted in the Globalmodel, since the large size of elements cannot accurately describe the orientation gradient. In contrast, subdivision becomes accessible when the element size is reduced in the Submodel, since the orientation gradient is further discretised into much more sections (or elements) in the Submodel and thus the description of orientation gradient is greatly improved. At point A, $\gamma_{\mathrm{b2-c2}}$ is much higher than $\gamma_{\mathrm{a2-d2}}$, and thus the primary microbands are along the b2-c2 direction (Fig.3d). Secondary microbands are supposed to develop between primary microbands, at point B for example. At point B, $\gamma_{\mathrm{b2-c2}}$ is slightly lower than $\gamma_{\mathrm{a2-d2}}$, and this means the secondary microbands are supposed to be along the a2-d2 direction if they developed, but the secondary microbands did not develop since the mesh resolution is still very low. This supposition of secondary microbands can be confirmed by the experimental observations in Fig.2c, where secondary microbands, along a2-d2 direction, developed between primary ones. The consistency between primary microbands (Fig.3d and e) and the most highly activated slip system (Fig.3b) shows the strong association between them [4].

In another ongoing research of authors, microbands developed when the element size in the Globalmodel was reduced to as small as that in the Submodel, as the results shown in the supplementary material. This is to say the formation of microbands is in nature. In reality, the deformation occurs at the scale of atoms, while the element size in the Submodel is still much larger (1.6 μm×1.6 μm). This is to say the prediction of microbands can also be influenced by the mesh resolution, and thus the prediction is only qualitative, but not quantitative. Increasing mesh resolution does enhance material flows [20]. The formation of microbands by varying the slip system activation and crystal rotation between domains benefits to the reduction of plastic work [21, 22], since microband formation is an energy effective deformation behaviour. It can be seen from reported experimental results that two sets of microbands develop when the shear strain/stress is low, e.g., plane strain compression [4] and deformation at the centre of this study. However, it is usually observed that one set of microbands is more prominent in rolled materials [3], since in rolling the shear strain/stress is high. The success of prediction of secondary microbands in the transition band (Fig.3e) is due to that the activation of the two sets of slip systems are almost equivalent (Fig.2b). In contrast, secondary microbands were not predicted in the Submodel of Region1 (Fig.3d) is

because of the great domination of the primary slip trace in this region. It is expected that the secondary microbands can be predicted after further increaseing the mesh resolution. The microbands in Fig.3d and e match well with the experimentally observed ones though the predicted microbands are more regular.

6. Summary

In this report, both experimental and numerical methods were used to characterize the microbands in rolled single crystals, and the predictions have been quantitatively validated by the experimental observations. Matrix bands were predicted in the Globalmodel, which formed by alternating slip activities and direction of crystal rotation through the thickness. At the lower scale, microbands were captured in the Submodel with greatly refined mesh, which were featured by variations of slip activities and crystal rotation between domains. These variations due to stress and strain fluctuation minimize plastic work.

Acknowledgements

This work was supported by Australian Research Council Discovery Project (DP170103092). The authors acknowledge use of facilities within the UOW Electron Microscopy Centre (LE0882613).

References

1. Raabe, D., et al., *Theory of orientation gradients in plastically strained crystals.* Acta Materialia, 2002. **50**(2): p. 421-440.
2. Rollett, A., et al., *Recrystallization and Related Annealing Phenomena: Second Edition*. Recrystallization and Related Annealing Phenomena: Second Edition. 2004. 1-628.
3. Liu, Q. and N. Hansen, *Macroscopic and microscopic subdivision of a cold-rolled aluminium single crystal of cubic orientation.* Proceedings of the Royal Society A: Mathematical, Physical and Engineering Sciences, 1998. **454**(1978): p. 2555-2591.
4. Afrin, N., et al., *Spatial orientations and structural irregularities associated with the formation of microbands in a cold deformed Goss oriented Ni single crystal.* Acta Materialia, 2012. **60**(18): p. 6288-6300.
5. Wert, J.A., *Macroscopic crystal rotation patterns in rolled aluminium single crystals.* Acta materialia, 2002. **50**(12): p. 3125-3139.
6. Rezvanian, O., M.A. Zikry, and A.M. Rajendran, *Microstructural modeling of grain subdivision and large strain inhomogeneous deformation modes in f.c.c. crystalline materials.* Mechanics of Materials, 2006. **38**(12): p. 1159-1169.

7. Wang, H., et al., *A crystal plasticity FEM study of through-thickness deformation and texture in a {112} <111> aluminium single crystal during accumulative roll-bonding.* Scientific Reports, 2019. **9**(1): p. 3401.
8. Dmitrieva, O., et al., *Lamination microstructure in shear deformed copper single crystals.* Acta Materialia, 2009. **57**(12): p. 3439-3449.
9. Wang, D., et al., *On the role of the collinear dislocation interaction in deformation patterning and laminate formation in single crystal plasticity.* Mechanics of Materials, 2018. **125**: p. 70-79.
10. Asaro, R.J., *CRYSTAL PLASTICITY.* Journal of Applied Mechanics, Transactions ASME, 1983. **50**(4 b): p. 921-934.
11. L.Bassani, J. and T.-Y. Wu, *Latent Hardening in Single Crystals II. Analytical Characterization and Predictions.* Proceedings of the Royal Society A: Mathematical, Physical and Engineering Sciences, 1991. **435**: p. 21.
12. Wang, H., et al., *Texture Modeling of Accumulative Roll-Bonding Processed Aluminum Single Crystal {1 2 3}<6 3 4> by Crystal Plasticity FE.* Advanced Engineering Materials, 2019. **21**(2): p. 1800827.
13. Wang, H., et al., *Coupled effects of initial orientation scatter and grain-interaction to texture evolution: a crystal plasticity FE study.* International Journal of Material Forming, 2019. **12**(1): p. 161-171.
14. Bachmann, F., R. Hielscher, and H. Schaeben, *Texture analysis with MTEX- Free and open source software toolbox*, in *Solid State Phenomena*. 2010. p. 63-68.
15. Guery, A., et al., *Slip activities in polycrystals determined by coupling DIC measurements with crystal plasticity calculations.* International Journal of Plasticity, 2016. **81**: p. 249-266.
16. Albou, A., J.H. Driver, and C. Maurice, *Microband evolution during large plastic strains of stable {110}〈112〉 Al and Al–Mn crystals.* Acta Materialia, 2010. **58**(8): p. 3022-3034.
17. Hurley, P.J., P.S. Bate, and F.J. Humphreys, *An objective study of substructural boundary alignment in aluminium.* Acta Materialia, 2003. **51**(16): p. 4737-4750.
18. Winther, G., X. Huang, and N. Hansen, *Crystallographic and macroscopic orientation of planar dislocation boundaries—correlation with grain orientation.* Acta Materialia, 2000. **48**(9): p. 2187-2198.
19. Winther, G., D.J. Jensen, and N. Hansen, *Dense dislocation walls and microbands aligned with slip planes—theoretical considerations.* Acta Materialia, 1997. **45**(12): p. 5059-5068.
20. Buchheit, T.E., G.W. Wellman, and C.C. Battaile, *Investigating the limits of polycrystal plasticity modeling.* International Journal of Plasticity, 2005. **21**(2): p. 221-249.
21. Petryk, H. and M. Kursa, *The energy criterion for deformation banding in ductile single crystals.* Journal of the Mechanics and Physics of Solids, 2013. **61**(8): p. 1854-1875.
22. Kuhlmann-Wilsdorf, D., *OVERVIEW No. 131"Regular" deformation bands (DBs) and the LEDS hypothesis.* Acta Materialia, 1999. **47**(6): p. 1697-1712.